

THE CYGNUS LOOP'S DISTANCE, PROPERTIES, & ENVIRONMENT DRIVEN MORPHOLOGY

ROBERT A. FESEN, KATHRYN E. WEIL & IGNACIO A. CISNEROS

6127 Wilder Lab, Department of Physics & Astronomy, Dartmouth College, Hanover, NH 03755, USA

WILLIAM P. BLAIR

Henry A. Rowland Department of Physics & Astronomy, Johns Hopkins University, 3400 N. Charles Street, Baltimore, MD 21218, USA

JOHN C. RAYMOND

Harvard-Smithsonian Center for Astrophysics, 60 Garden St., Cambridge, MA 02138, USA

Accepted to MNRAS

ABSTRACT

The Cygnus Loop is among the brightest and best studied evolved Galactic supernova remnants. However, its distance has remained uncertain thus undermining quantitative understanding about many of its fundamental properties. Here we present moderate-dispersion spectra of stars with projected locations toward the remnant. Spectra of three stars revealed Na I 5890,5896 Å and Ca II 3934 Å absorption features associated with the remnant's expanding shell, with velocities ranging from -160 to $+240$ km s $^{-1}$. Combining Gaia DR2 parallax measurements for these stars with other recent observations, we find the distance to the Cygnus Loop's centre is 735 ± 25 pc, only a bit less than the 770 pc value proposed by Minkowski some 60 years ago. Using this new distance, we discuss the remnant's physical properties including size, SN explosion energy, and shock velocities. We also present multi-wavelength emission maps which reveal that, instead of being located in a progenitor wind-driven cavity as has long been assumed, the Cygnus Loop lies in an extended, low density region. Rather than wind-driven cavity walls, these images reveal in unprecedented clarity the sizes and locations of local interstellar clouds with which the remnant is interacting, giving rise to its large-scale morphology.

Subject headings: ISM: individual (Cygnus Loop) - ISM: kinematics and dynamics - ISM: supernova remnants

1. BACKGROUND

The Galactic supernova remnant (SNR) G74.0-8.5, commonly known as the Cygnus Loop or Veil Nebula, is thought to be a middle-age remnant with an estimated age of $1-2 \times 10^4$ yr. Based on extensive multi-wavelength observations, the Cygnus Loop has been most often modeled as the remnant of a supernova explosion that occurred inside an interstellar cavity likely created by a high-mass progenitor star (McCray & Snow 1979; Hester et al. 1994; Levenson et al. 1997, 1998; Miyata & Tsunemi 1999; Fang et al. 2017).

Underlying any quantitative analysis of the Cygnus Loop is uncertainty about its distance. For many decades, the most often adopted value was a kinematic investigation by Minkowski (1958). Hubble (1937) measured a proper motion of $0''.03$ yr $^{-1}$ for the remnant's bright eastern and western nebulae (see Fig. 1). This value, when combined with an average radial velocity of 115 km s $^{-1}$ for the remnant's optical filaments, led Minkowski (1958) to estimate a distance of 770 pc.

However more recent distance estimates have ranged from 440 to 1400 pc (see review by Fesen et al. 2018). The most cited value is 540^{+100}_{-80} pc by Blair et al. (2005). Although smaller than many other estimates, this distance appeared in line with a subsequent study which estimated a distance of 576 ± 61 pc to a sdO star, KPD 2055 +3111, lying in the direction of the remnant's eastern nebulosities (Blair et al. 2009).

Because this star's UV spectrum showed high-velocity O VI 1032 Å line absorption, Blair et al. (2009) argued the star must be behind the remnant thus limiting the remnant's distance to less than $\simeq 576$ pc. However, Gaia DR2 data (Gaia Collaboration et al. 2018) report a parallax of 1.2610 ± 0.0413 mas and hence a distance of 793 ± 30 pc for this star (Table 1).

Other recent distance estimates have tended to favor larger values. Medina et al. (2014) used spectra of Balmer-dominated H α filaments to estimate shock velocities of around 400 km s $^{-1}$ based on H α emission profiles. Combined with proper motions by Salvesen et al. (2009), they deduced a distance of around 890 pc. However, a re-analysis of thermal equilibrium in a collisionless shock led to a reduction of the derived shock velocities which decreased the remnant's estimated distance to $\simeq 800$ pc (Raymond et al. 2015).

The most recent distance estimate to the Cygnus Loop is that of Fesen et al. (2018) who suggested optical nebulosities around two stars were stellar mass-loss material interacting with the remnant's expanding shock front and thus could be used to estimate the Cygnus Loop's distance. A small emission-line nebula with a bow-shaped morphology centred on a M4 III star, J205601, near the remnant's eastern nebula NGC 6992 was shown to be shock-heated with significantly higher electron densities than typically seen in the remnant's filaments. Since distance estimates to this red giant ranged from 1.0 to 4.2

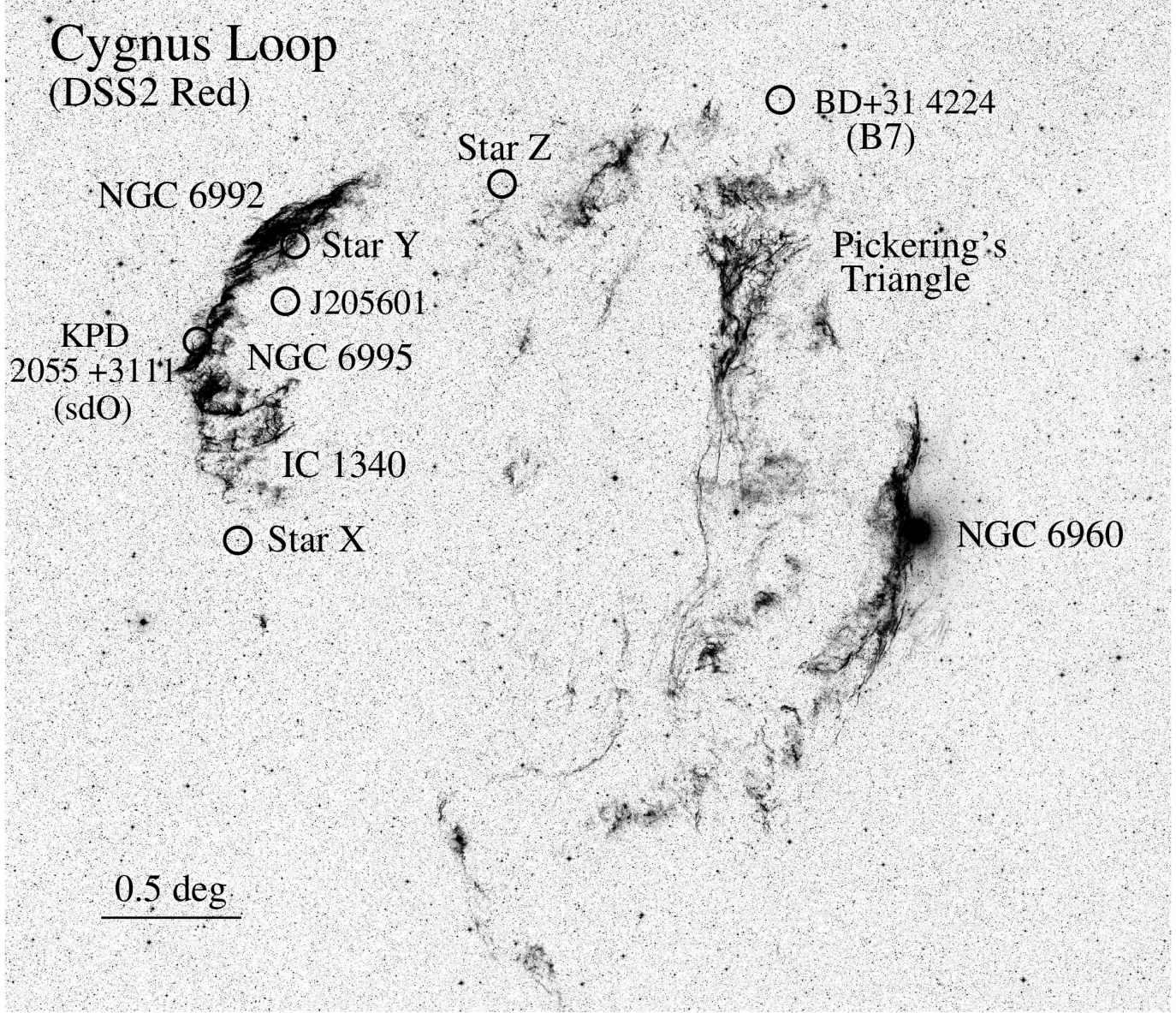


FIG. 1.— Reproduction of the red image of the Digital Sky Survey of the Cygnus Loop. Marked are our three program stars X, Y, and Z, along with the Blair et al. (2009) sdO star (KPD 2055 +3111), and the two stars, J205601 & BD+31 4224, suspected by Fesen et al. (2018) to be physically interacting with the remnant's shock front. North is up, East to the left.

TABLE 1
STARS USED TO ESTIMATE THE DISTANCE TO THE CYGNUS LOOP

| Star ID ^a | Catalog Number ^b | RA (J2000) | Dec (J2000) | Magnitude (v) | Gaia DR2 Parallax | Gaia DR2 Distance | Location to SNR |
|----------------------|-----------------------------|--------------|--------------|---------------|-------------------------|-------------------|-----------------|
| J205601 | TYC 2688-1037-1 | 20:56:00.936 | +31:31:29.75 | 11.57 | 0.6334 ± 0.0661 mas | 1580 ± 180 pc | far behind |
| KPD 2055 +3111 | UCAC2 42838052 | 20:57:26.889 | +31:22:52.56 | 14.12 | 1.2610 ± 0.0413 mas | 793 ± 30 pc | behind |
| BD+31 4224 | TYC 2691-290-1 | 20:47:51.817 | +32:14:11.33 | 9.58 | 1.3033 ± 0.0438 mas | 767 ± 27 pc | inside |
| Star X | HD 335334 | 20:56:44.629 | +30:41:14.33 | 9.51 | 1.3586 ± 0.0440 mas | 736 ± 25 pc | just behind |
| Star Y | TYC 2688-365-1 | 20:55:51.948 | +31:43:27.40 | 11.25 | 1.3598 ± 0.0449 mas | 735 ± 25 pc | just behind |
| Star Z | TYC 2692-3378-1 | 20:52:27.557 | +31:56:29.48 | 10.73 | 1.1581 ± 0.0390 mas | 864 ± 30 pc | far behind |

^a References: J205601 & BD+31 4224: Fesen et al. (2018); KPD 2055 +3111: Blair et al. (2009); X, Y, Z: this work

^b TYC: Høg et al. (2000); UCAC2: Zacharias et al. (2004); HD: Henry Draper Catalogue

kpc, Fesen et al. (2018) struggled to connect this star and the nebulosity to the remnant. Gaia’s DR2 parallax of 0.6334 ± 0.0661 mas implies a distance around 1.6 kpc kpc, placing it well behind the remnant (Table 1), leaving the origin of the bow-shaped nebulosity somewhat of a mystery.

Fesen et al. (2018) also identified a B7 V star, BD+31 4224, located along the remnant’s northwestern limb within a small arc of nebulosity in a complex region of curved and distorted filaments suggestive of a disturbance of the remnant’s shock front due to the B star’s stellar winds. Whereas Fesen et al. (2018) estimated the star’s distance to be 0.8 to 1.0 kpc, Gaia DR2 reports a parallax of 1.3033 ± 0.0438 mas implying a distance of 767 ± 35 pc (Table 1).

This distance estimate, when taken together with the Blair et al. (2009) sdO star lying behind the remnant, suggests a firm distance limit of less than 800 pc, consistent with Minkowski’s 1958 value of 770 pc. A distance $\simeq 750$ - 800 pc could explain the failure by Welsh et al. (2002) to detect high-velocity Na I and Ca II line absorptions associated with the remnant in several stars located along the line-of-sight to the Cygnus Loop at distances less than ~ 700 pc.

In light of the recent Gaia data release giving relatively accurate distances to many earlier type stars located toward the Cygnus Loop, we obtained optical spectra of several stars located between 700 and 900 pc in the remnant’s direction to search for associated high-velocity Na I and Ca II absorption features as additional clues to the remnant’s distance. Our spectral observations are described in §2, with results presented in §3. Combining these new data with prior observations, we discuss in §4 the Cygnus Loop’s likely distance and thus its true size and supernova energy. We also present multi-wavelength images which reveal the remnant’s likely interactions with several local interstellar clouds leading to a re-assessment of the long assumed progenitor wind-driven cavity model. Our conclusions are summarized in §5.

2. OBSERVATIONS

Roughly two dozen stars were selected as spectroscopic program targets on the basis of Gaia determined distances between 700 and 950 pc, $m_g < 13.5$, Gaia T_{eff} values greater than 8000 K, and projected locations within the Cygnus Loop’s optical boundaries. Many had early-type A classifications listed on SIMBAD (Wenger et al. 2000). This modest target list was viewed as sufficiently large to uncover at least a few background stars exhibiting high-velocity interstellar absorption components associated with the Cygnus Loop.

Moderate-dispersion spectra of several of these stars were observed on 2018 May 30, 31 and June 1, 2, and 3 with the 1.3m McGraw-Hill telescope at MDM Observatory located at Kitt Peak, Arizona. The data were taken using a Boller & Chivens Spectrograph (CCDS) which employs a Loral 1200×800 CCD detector. We used an $1800 \text{ grooves mm}^{-1}$ grating blazed at 4700 \AA to yield a wavelength coverage of 330 \AA with a spectral scale of 0.275 \AA per pixel. Exposure times varied from $1 - 2 \times 1200$ s to 2×3000 s depending on star brightness and wavelength coverage.

A 1.5 arcsec wide slit was used which resulted in a mea-

sured FWHM of 2.2 pixels, corresponding to a spectral resolution of 0.61 \AA , providing an effective $R \simeq 9700$ at the Na I 5890,5996 \AA lines and $R \simeq 6500$ at the Ca II K 3934 \AA line. Although these spectral resolutions are low relative to conventional interstellar absorption studies where R values typically exceed 30,000, this spectrograph + grating system provided velocity resolutions ≈ 30 and 45 km s^{-1} for the Na I and Ca II lines, respectively. This was judged adequate for detecting the expected high-velocity expansion filaments, in the range of 50 to 300 km s^{-1} , in the spectrum of background stars.

Standard pipeline data reduction was performed using IRAF¹. The spectra were bias-subtracted, cosmic-ray corrected using the L.A. Cosmic software (van Dokkum 2001), co-added, wavelength calibrated using Hg, Ne, Ar, and Xe comparison lamps, and have been corrected to local standard of rest (LSR) values. Detected interstellar Na I and Ca II line components were deblended using IRAF Gaussian fitting routines. Measured velocities have a typical uncertainties of $\pm 5 \text{ km s}^{-1}$.

3. RESULTS

Although our program stars were distributed across the remnant, only three stars located in eastern half were found to exhibit high-velocity absorption components visible given our spectral resolution and S/N. Projected locations of these three stars, labeled X, Y, and Z are shown in Figure 1 along with the locations of the sdO star KPD 2055 +3111 (hereafter KPD) studied by Blair et al. (2009) and the two stars J205601 (M4 III) and BD+31 4224 (B7 V) discussed by Fesen et al. (2018). Coordinates and Gaia parallax measurements for all six stars are listed in Table 1. While we were unable to classify our three observed program stars due to our limited spectral coverage, Stars X, Y, and Z have $B - V$ values of 0.03, 0.08, and 0.29 with Star X classified as A0 (Wenger et al. 2000).

Reduced and normalized spectra of Stars X, Y, and Z for the wavelength region around the Na I D lines at 5889.95 and 5895.92 \AA are showed in Figure 2. Measured D1 and D2 absorption component velocities and equivalent widths are listed in Table 2.

The spectrum of the 9.5 mag Star X located south of NGC 6995 and IC 1340 exhibited the cleanest high-velocity absorption components, showing both red and blue absorption features. Deconvolution of the observed Na I profiles indicates high-velocity interstellar components at $\simeq -60$ and $+95 \text{ km s}^{-1}$ (Fig. 2; upper panels). With a Gaia estimated distance of 736 ± 25 pc, the detection of both red and blue shifted Na I features in this star’s spectrum implies a distance limit to the backside of the Cygnus Loop of less than $\simeq 760$ pc.

Star X’s spectrum covering the Ca II K line at 3933.66 \AA is shown in Figure 3. As expected due to interstellar grain destruction releasing refractory Ca atoms following SN shock passage (Routly & Spitzer 1952), the strength of the high-velocity Ca II absorption features are noticeably stronger here relative to the low-velocity interstellar features compared to that seen for Na I (Fig. 2).

¹ IRAF is distributed by the National Optical Astronomy Observatories, which is operated by the Association of Universities for Research in Astronomy, Inc. (AURA) under cooperative agreement with the National Science Foundation.

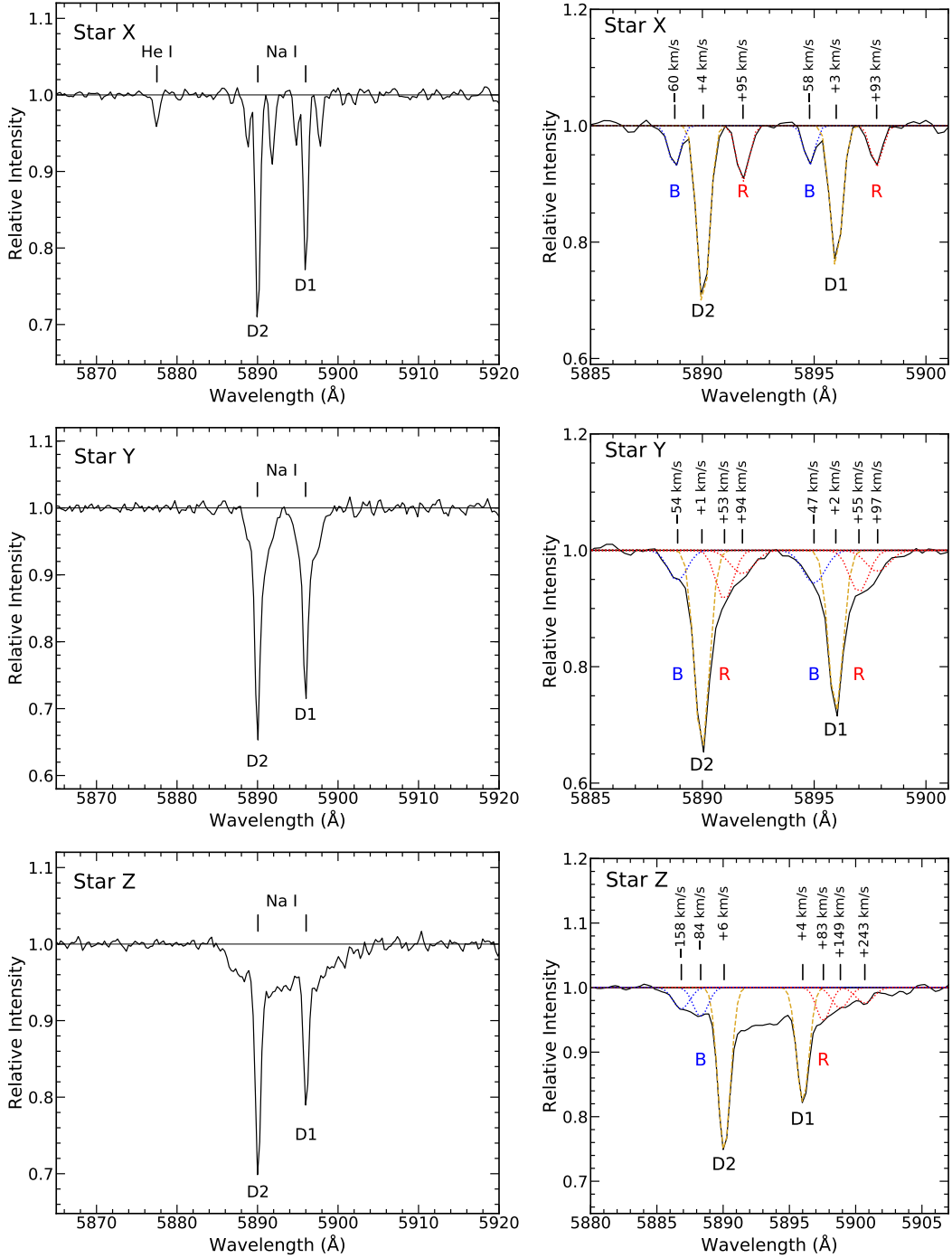


FIG. 2.— Spectra covering the Na I D line region for Stars X, Y, and Z.

The spectrum of Star Y with a projected location just west of the remnant’s bright nebula NGC 6992 also showed red and blue high-velocity interstellar components indicating it too must lie behind the remnant (Fig. 2; middle panels). Components with approximate LSR velocities of -50 , $+50$, & $+95$ km s $^{-1}$ are seen for both D1 and D2 lines.

With a Gaia reported distance nearly identical to that of Star X, namely 735 ± 25 pc, Star Y’s spectrum strengthens a maximum distance limit to the backside of the Cygnus Loop of $\simeq 760$ pc. However, since both stars are located near the remnant’s eastern limb, a distance

limit to the centre of the remnant must take into account the spherical curvature and any aspherical geometry of the Cygnus Loop.

Lastly, the spectrum of Star Z, a 10.7 mag late A/early F star located near the remnant’s north-central limb, showed the broadest and most complicated system of Na I absorption lines (Fig. 2; lower panels). At least five high-velocity Na I D1 and D2 absorption features are detected with velocities ranging from -158 ± 5 to $+243 \pm 5$ km s $^{-1}$. Both for clarity and limited by our spectral resolution, we have chosen not to show deconvolved components for the overlapping region in between

TABLE 2
MEASURED INTERSTELLAR VELOCITY COMPONENTS AND EQUIVALENT WIDTHS

| Star ID | Line | V_0 km s $^{-1}$ | EW_0 Å | V_{B1} km s $^{-1}$ | EW_{B1} Å | V_{B2} km s $^{-1}$ | EW_{B2} Å | V_{R1} km s $^{-1}$ | EW_{R1} Å | V_{R2} km s $^{-1}$ | EW_{R2} Å | V_{R3} km s $^{-1}$ | EW_{R3} Å |
|---------|---------|-----------------------|-------------|--------------------------|----------------|--------------------------|----------------|--------------------------|----------------|--------------------------|----------------|--------------------------|----------------|
| Star X | Na I D1 | +3 | 0.17 | -58 | 0.04 | ... | ... | +93 | 0.05 | ... | ... | ... | ... |
| | Na I D2 | +4 | 0.22 | -60 | 0.05 | ... | ... | +95 | 0.07 | ... | ... | ... | ... |
| | Ca II K | -2 | 0.13 | -58 | 0.11 | ... | ... | +88 | 0.29 | ... | ... | ... | ... |
| Star Y | Na I D1 | +2 | 0.23 | -47 | 0.07 | ... | ... | +55 | 0.08 | +97 | 0.05 | ... | ... |
| | Na I D2 | +1 | 0.29 | -54 | 0.06 | ... | ... | +53 | 0.08 | +94 | 0.05 | ... | ... |
| Star Z | Na I D1 | +4 | 0.21 | ... | ... | ... | ... | +83 | 0.07 | +149 | 0.05 | +243 | 0.04 |
| | Na I D2 | +6 | 0.30 | -84 | 0.06 | -158 | 0.05 | ... | ... | ... | ... | ... | ... |

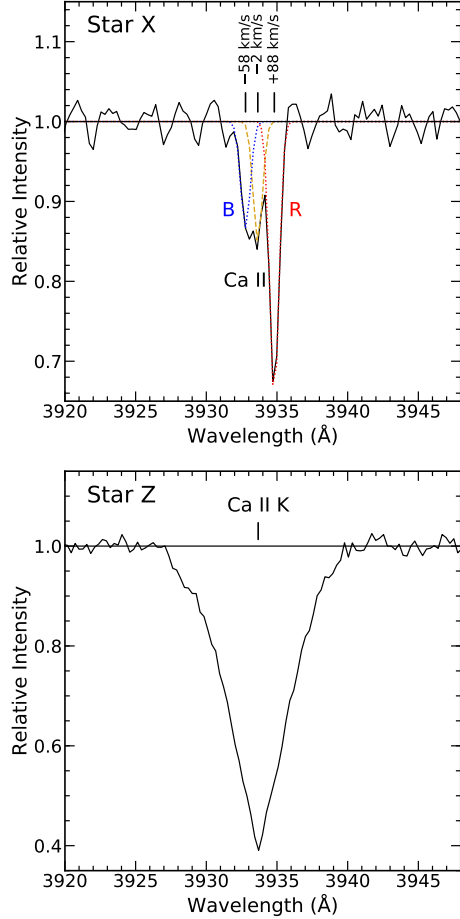


FIG. 3.— Spectra covering the Ca II line region for Stars X and Z.

the D1 and D2 lines. At Star Z’s estimated distance of 864 ± 30 pc, the detection of these many blue and red shifted Na I D1 and D2 absorption features is consistent with a maximum backside remnant distance limit of 760 pc set by Stars X and Y.

A spectrum of Star Z covering the Ca II K line is shown in Figure 3. Although our spectral resolution and S/N at 3934 Å is too low to resolve the expected individual high-velocity interstellar Ca components from the stellar Ca II absorption profile, there are hints of some components along the edges of the profile’s blue and red wings.

4. DISCUSSION

4.1. The Cygnus Loop’s Distance

A previous search for high-velocity components associated with the remnant conducted by Welsh et al. (2002) likely failed due to their selection of stars with distances less than ~ 700 pc. However, spectra of stars with distance in excess of 700 pc presented in Figures 2 and 3 show clear evidence for high-velocity interstellar Na I and Ca II absorptions from the Cygnus Loop’s expanding shell.

In addition to the relatively high red and blue radial velocities detected for Na I lines in the spectra of Stars X, Y, and Z, the decreased ratio of Na I D1/Ca II K equivalent widths in Star X is consistent with these components arising from shocked gas and subsequent grain destruction in accord with the well-established Routly-Spitzer effect (Routly & Spitzer 1952; Vallerga et al. 1993). Whereas the D1/K EW ratio is 1.3 for the low velocity component in the spectrum of Star X, the D1/K ratio is only 0.36 and 0.17 for the -60 and $+95$ km s $^{-1}$ components. Although we did not measure the Ca II equivalent widths for Stars Y and Z, their high-velocity Na I components are as large or larger than that seen in Star X and hence would be expected to exhibit strong high-velocity Ca II absorptions with corresponding low D1/K equivalent width ratios.

The detection of both blue and red high-velocity interstellar absorption features in the spectra of Stars X and Y with Gaia estimated distances of 735 ± 25 pc, together with several blue and red shifted interstellar absorptions in Star Z located at 864 pc, place a firm maximum distance limit to the backside of the Cygnus Loop of 760 pc. This is consistent with the KPD star’s 793 ± 30 pc distance which showed remnant related line absorptions in its UV spectrum implying a location behind the remnant (Blair et al. 2009).

Formally, these detections allow for all distances less than 760 pc for the backside of the remnant including the $\simeq 550$ pc estimate proposed by Blair et al. (2009). However, if the stellar wind from the B7 star, BD+31 4224, located along the remnant’s northwestern limb is truly interacting with the remnant’s expanding shock wave as argued by Fesen et al. (2018), then its Gaia estimated distance of 767 ± 27 pc places severe constraints on the remnant’s distance.

Adopting the premise that the B7 star is interacting with the remnant, this effectively anchors the Cygnus Loop to distances within the B7 star’s parallax measurement errors; namely, the remnant’s rear hemisphere can be no closer than 740 pc, and its frontside can be no further than 794 pc. At such distances, the Cygnus Loop’s main shell diameter of 2.85 degrees implies a linear di-

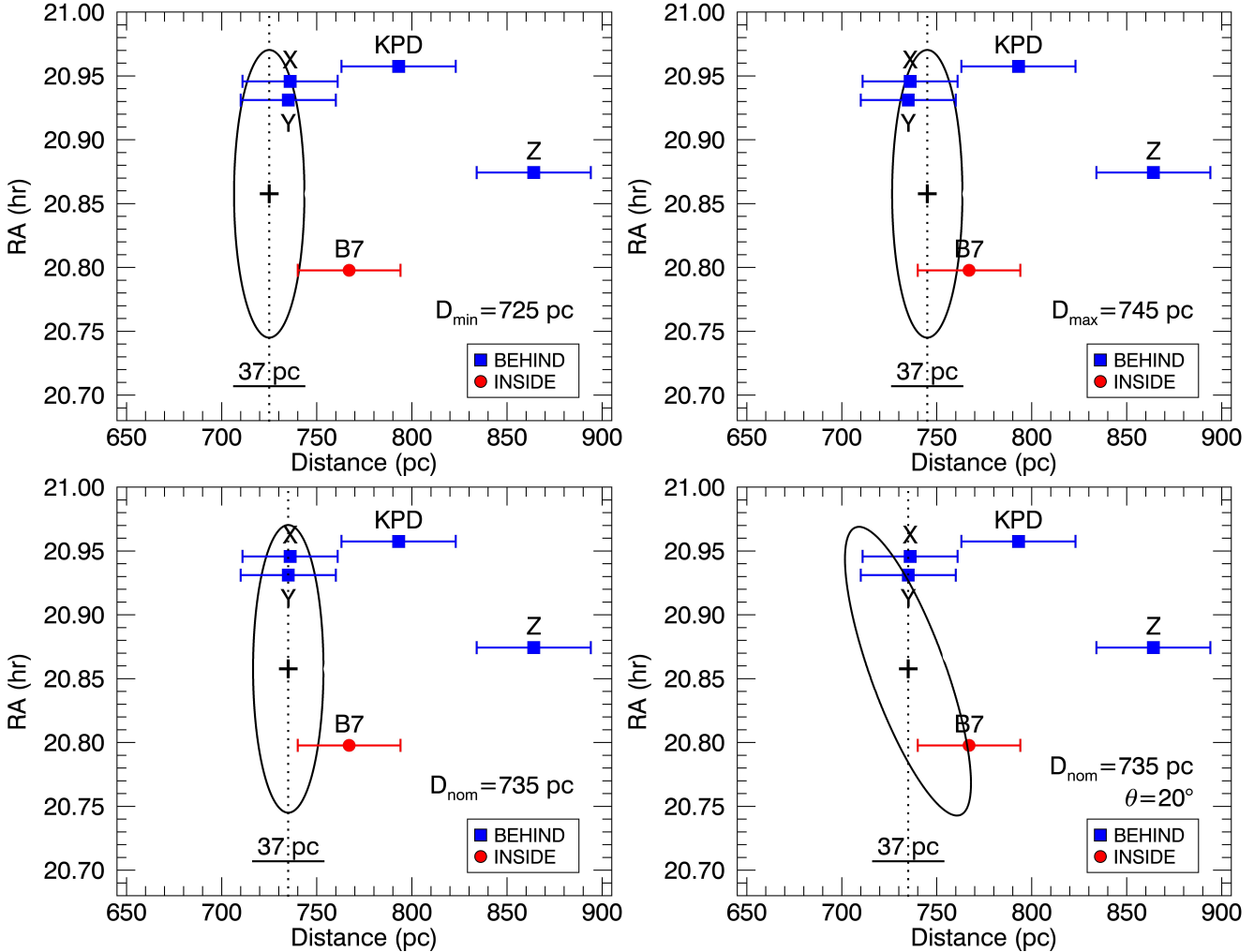


FIG. 4.— Plots of Gaia distances vs. RA for Stars X, Y, and Z plus KPD and the B7 star with the ellipse representing the slightly aspherical remnant. The blue squares represent stars behind the remnant, while the red circle represents the B7 star that resides inside the remnant. The cross represents the location of the centre of the remnant. **Upper Left:** Minimum distance to the remnant while having the B7 star located inside the remnant. **Upper Right:** Maximum distance to the remnant while having Star Y located behind the remnant. **Lower Left:** Nominal distance to the remnant from the average of the minimum and maximum distances. **Lower Right:** Nominal distance with a tilted oblate spheroid geometry for the remnant, such that Stars X and Y are located behind the remnant while the B7 star is located inside the remnant at their nominal distances.

ameter of $\simeq 37$ pc.

The combination of the B7 star interacting with the remnant's northwestern hemisphere and the requirement that both Stars X and Y at 735 pc must lie behind the remnant places additional constraints on the maximum and minimum distances to the Cygnus Loop's centre of expansion. Measured from its optical emission structure, the remnant is slightly asymmetric corresponding to an ellipse in the distance versus RA plane. Figure 4 shows plots of Gaia distances versus RA for Stars X, Y, Z, plus KPD, and the B7 star. Stars that must lie behind the remnant are shown as blue squares, while the B7 star which must be inside or interacting with the backside of the remnant is shown as a red circle. The projection of the remnant, centred at 20.854 hours RA (J2000: 20:51:14), in distance vs. RA is illustrated in these four plots.

The top left panel of Figure 4 shows that an aspherical remnant at a distance of 725 pc is just barely able to intersect the B7 star at its Gaia shortest estimated dis-

tance, thereby setting a minimum distance to the Cygnus Loop's centre at 725 pc. In similar fashion, the top right panel shows that this same 37 pc diameter remnant cannot be centred any farther away than $\simeq 745$ pc so as to have Stars X and Y behind the remnant's rear shell at their maximum Gaia estimated distances.

The fortuitous situation of having two stars, namely Stars X and Y, located behind the remnant's eastern limb at virtually the same distance (735 pc) suggests the remnant's rear eastern hemisphere is likely to be close to this 735 pc value. However, no Cygnus Loop distance between the 725 and 745 pc limits discussed above can simultaneously fulfill the requirements that Stars X and Y lie behind a 37 pc diameter remnant at their nominal Gaia 735 pc value while still having the B7 star inside or just touching the remnant's rear NW shell at its nominal 767 pc distance. This is illustrated in the lower left panel.

A solution is that the Cygnus Loop's main northern shell containing its brightest nebulae is aspherical and tilted. As shown in the lower right panel of Figure 4, if

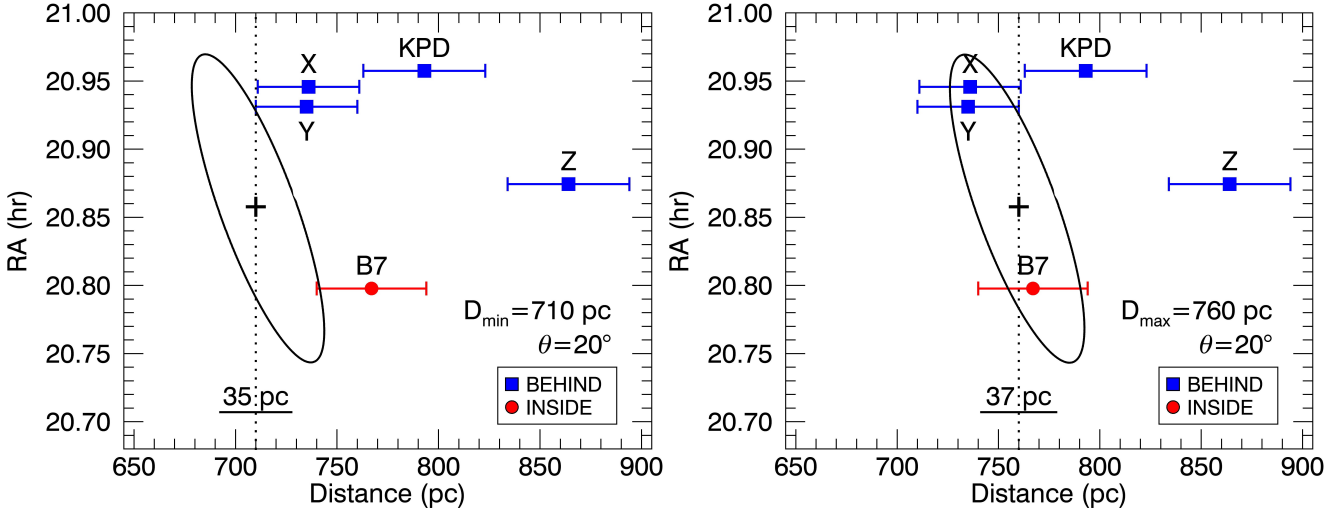


FIG. 5.— Similar plots to those shown in Figure 4. **Left Panel:** Minimum distance of 710 pc to the remnant for a 20 degree tilt such that the B7 remains inside the remnant at its extrema distance while Stars X and Y are behind the remnant. **Right Panel:** Maximum distance of 760 pc to the remnant for 20 degree tilt such that Stars X and Y lie behind the remnant at their extrema distances while the B7 star lies within the remnant.

the remnant's eastern half is tilted toward us then the various stellar distances would be in better agreement; that is, the B7 star could lie inside the remnant's NW limb while having Stars X and Y behind the remnant's eastern limb.

If true, this might imply the remnant's eastern limb expanded more rapidly towards us. Consequently the remnant's western limb, particularly its northwestern limb, is located farther away. Specifically, an asymmetric remnant with a diameter $\simeq 37$ pc tilted some 20 degrees allows Stars X and Y to lie behind the remnant's eastern limb while still having the B7 star within the remnant. A mild asymmetry along our line of sight would be consistent with *Suzaku* and *XMM-Newton* X-ray studies of the remnant (Uchida et al. 2009).

Although larger asymmetries or tilts are possible, the remnant's fairly circular projected morphology in its main shell of emission suggests large departures from symmetry are unlikely. Thus, adopting an effective maximum tilt of 20 degrees, the plots shown in Figure 5 suggest more realistic distance limits to the remnant. In the left panel, a 35 pc diameter remnant tilted 20 degrees whose east and west limbs match the observed Cygnus Loop's dimensions cannot be closer than 710 pc and still have the B7 star in physical contact with the remnant. A maximum distance for a 20 degree tilt of 760 pc is shown in the right panel of this figure, where Star Y is at its maximum distance while still lying behind the remnant.

Consequently, from the analyses discussed above, we conclude the centre of the main, northern portion of the Cygnus Loop containing the majority of the remnant's bright optical nebulae lies at a distance of 735 ± 25 pc with distances between 735 and 745 pc slightly favored based on the B7 star's nominal 767 pc distance. Interestingly, this distance estimate is only a bit less than the 770 pc value proposed by Minkowski some 60 years ago. At 735 pc, the remnant's angular diameter of 2.88 degrees corresponds to $\simeq 37$ pc with an uncertainty of just a few parsecs due to the remnant's degree of asphericity.

4.2. The Cygnus Loop's Fundamental Properties

Assuming our distance estimate of 735 pc to the remnant's centre and its east-west diameter of 37 pc, we list in Table 3 several basic properties of the Cygnus Loop including shock velocities in low density regions, in slightly denser regions where the shock is transitioning from non-radiative Balmer dominated filament emission to radiative, and finally in denser cloud regions. As seen in this table, we find good agreement with spectroscopically inferred shock velocities for the three different density regions using the new distance estimate.

A distance of 735 pc implies a lower SN energy of $0.7 \pm 0.2 \times 10^{51}$ erg than the canonical SN explosion energy of $1-2 \times 10^{51}$ erg. This value is similar to earlier estimates of $E_0 = 3-7 \times 10^{50} (d_{pc}/770)^{5/2}$ erg using Minkowski's distance of 770 pc (Rappaport et al. 1974; Falle & Garlick 1982; Ballet et al. 1984; Miyata & Tsunemi 1999). However, these previous estimates, as well as ours, do not include the remnant's southern breakout region which would raise the E_0 value a bit, possibly close to 1×10^{51} erg (see discussion in §4.4).

4.3. The Remnant's Environment Driven Morphology

An improved knowledge about the Cygnus Loop's distance can help our understanding about its local environment and how this has impacted the remnant's gross morphology and emission structure. Below, we briefly review past conclusions regarding the remnant's interstellar environment and evolution, specifically its proposed origin as a progenitor wind-blown cavity explosion. We then present multi-wavelength emission maps that offer a new look into the remnant's interstellar environment as the origin of the remnant's large-scale structure.

4.3.1. A Historical Perspective

As seen across many wavelengths, the Cygnus Loop's overall morphology is far from that expected for an expanding sphere in a uniform medium. Its northern portion is dominated by bright and nearly opposing nebulae, NGC 6960 in the west and NGC 6992 & NGC 6995 in the east (see Fig. 1). In addition, there is an extensive

TABLE 3
FUNDAMENTAL PROPERTIES OF THE CYGNUS LOOP

| Property | Value | Details & References |
|----------------------------|--|--|
| Distance and Size | | |
| Distance | 735 \pm 25 pc | based on Gaia DR2 parallax measurements of several stars: this paper |
| Diameter | E-W 37 \pm 2 pc N-S 47 \pm 3 pc | adopting a 735 pc distance and an E-W diameter of 2.88 degrees: this paper adopting a 735 pc distance and a N-S diameter of 3.65 degrees: this paper |
| Blast Wave | | |
| n_0 | 0.4 \pm 0.1 cm $^{-3}$ | from Balmer filaments and optical depth of O VI: Raymond et al. (2003) |
| Proper Motion | 0.100 \pm 0.025'' yr $^{-1}$ | mean value for 18 positions: Salvesen et al. (2009) |
| V_{shock} | 348 \pm 87 km s $^{-1}$ | combining 735 pc distance and Balmer filament proper motions: this paper 343 \pm 26 km s $^{-1}$: Medina et al. (2014); 360 km s $^{-1}$: Raymond et al. (2015) |
| Sedov | | |
| Age | 21,000 \pm 4,000 yr | $t = 0.4 \times \text{radius}/348 \pm 87 \text{ km s}^{-1}$: this paper |
| E | 0.7 \pm 0.2 $\times 10^{51}$ erg | $n_0 = 0.4 \pm 0.1 \text{ cm}^{-3}$; radius = $1.54 \times 10^{19} \text{ cm} E_{51}^{1/5} n_0^{-1/5} t_{1000}^{2/5}$ yr |
| V_{shock} | 367 \pm 80 km s $^{-1}$ | $V = 1950 \text{ km s}^{-1} E_{51}^{1/5} n_0^{-1/5} t_{1000}^{-3/5}$ yr |
| Transitioning Shock | | |
| n_0 | 1.5 \pm 0.5 cm $^{-3}$ | Long et al. (1992) |
| Proper Motion | 0.070 \pm 0.008'' yr $^{-1}$ | northeastern Balmer filament transitioning to radiative: Blair et al. (2005) |
| V_{shock} | 244 \pm 28 km s $^{-1}$ | combining 735 pc distance & filament proper motion: this paper |
| Cloud Shock | | |
| n_0 | $\simeq 3 - 10 \text{ cm}^{-3}$ | Raymond et al. (1988); Levenson et al. (1998); Leahy (2003); McEntaffer & Brantseg (2011) |
| Proper Motion | 0.030 - 0.040'' yr $^{-1}$ | Hubble (1937); Shull & Hippelien (1991) |
| V_{shock} | 105 - 140 km s $^{-1}$ | combining 735 pc distance and filament proper motion: this paper Minkowski (1958) & Doroshenko (1970) find 110 to 115 km s $^{-1}$ for bright filaments |

complex of emission filaments along its north-central region (Pickering's Triangle) with numerous other smaller nebulae and filaments, all surrounded by a nearly complete X-ray emitting and Balmer-dominated shock front shell.

Fainter and much sparser optical, X-ray, and radio emissions extending some 90 arcminutes to the south from the remnant's nominal centre mark a prominent rupture-like structure best seen in X-rays (Levenson et al. 1997; Aschenbach & Leahy 1999). This 'blowout region' exhibits such different radio polarization properties that it has led some to propose it to be a separate SNR (Uyaniker et al. 2002; Sun et al. 2006; West et al. 2016).

The idea that the Cygnus Loop is a progenitor cavity explosion goes back to the earliest X-ray studies of the remnant. The discovery by Tucker (1971) that the remnant's X-ray inferred blast wave velocity was almost three times the velocity of the optical filaments, led McKee & Cowie (1975) to suggest the remnant's bright optical nebulae are due to dense interstellar clouds recently hit by the blast wave.

This notion was subsequently questioned by McCray & Snow (1979), Charles et al. (1985), and Braun & Strom (1986) who viewed such a scenario as unlikely to have created 'such a nicely spherical shell'. They instead suggested that the Cygnus Loop's shape was the result of a SN explosion taking place in a largely spherical, wind-driven cavity pre-dating the SNR, produced by the SN progenitor itself.

There has been considerable support for the Cygnus Loop being a cavity explosion remnant. Spectral X-ray analyses revealed evidence for a high-mass progenitor through observed enrichments of O, Ne, and Mg suggesting ejecta from a \simeq 15 solar mass core-collapse SN. In

addition, numerous model investigations have concluded that the remnant's properties are consistent with a SN explosion inside an interstellar cavity created by the progenitor star (Hester et al. 1994; Graham et al. 1995; Levenson et al. 1998; Uchida et al. 2009). Recently, Fang et al. (2017) conducted 3D hydrodynamic simulations assuming an anisotropic and latitude-dependent progenitor wind and achieved good agreement with the remnant's observed morphology.

However, it's been known since the early 1920's, even before it was realized to be a SN remnant, that the Cygnus Loop's bright western nebula, NGC 6960, marks the boundary of a significant drop off in star density farther to the west due to an adjacent interstellar cloud (Wolf 1923; Duncan 1923; Oort 1946). This difference is now understood as dust destruction by the remnant's blast wave. Obscuration caused by this cloud is readily apparent on photographic images of NGC 6960 such as those published by Ross (1931).

Extinction differences around NGC 6960 have been studied by Chamberlain (1953) and Bok & Warwick (1957), with H I and CO emission maps of the region showing a good correlation with the observed optical obscuration (de Noyen 1975; Scoville et al. 1977). While an analysis of mid-infrared images of the remnant and its local interstellar environment led Arendt et al. (1992) to suggest no direct link between this western cloud and NGC 6960, a study of X-ray and optical emissions along the Cygnus Loop's western limb led Levenson et al. (1996, 1998) to conclude the remnant was, in fact, directly interacting with this cloud.

Observations revealing an expanding shell of neutral hydrogen along the Cygnus Loop's northeastern limb led Leahy (2003) to suggest the presence of an interstellar

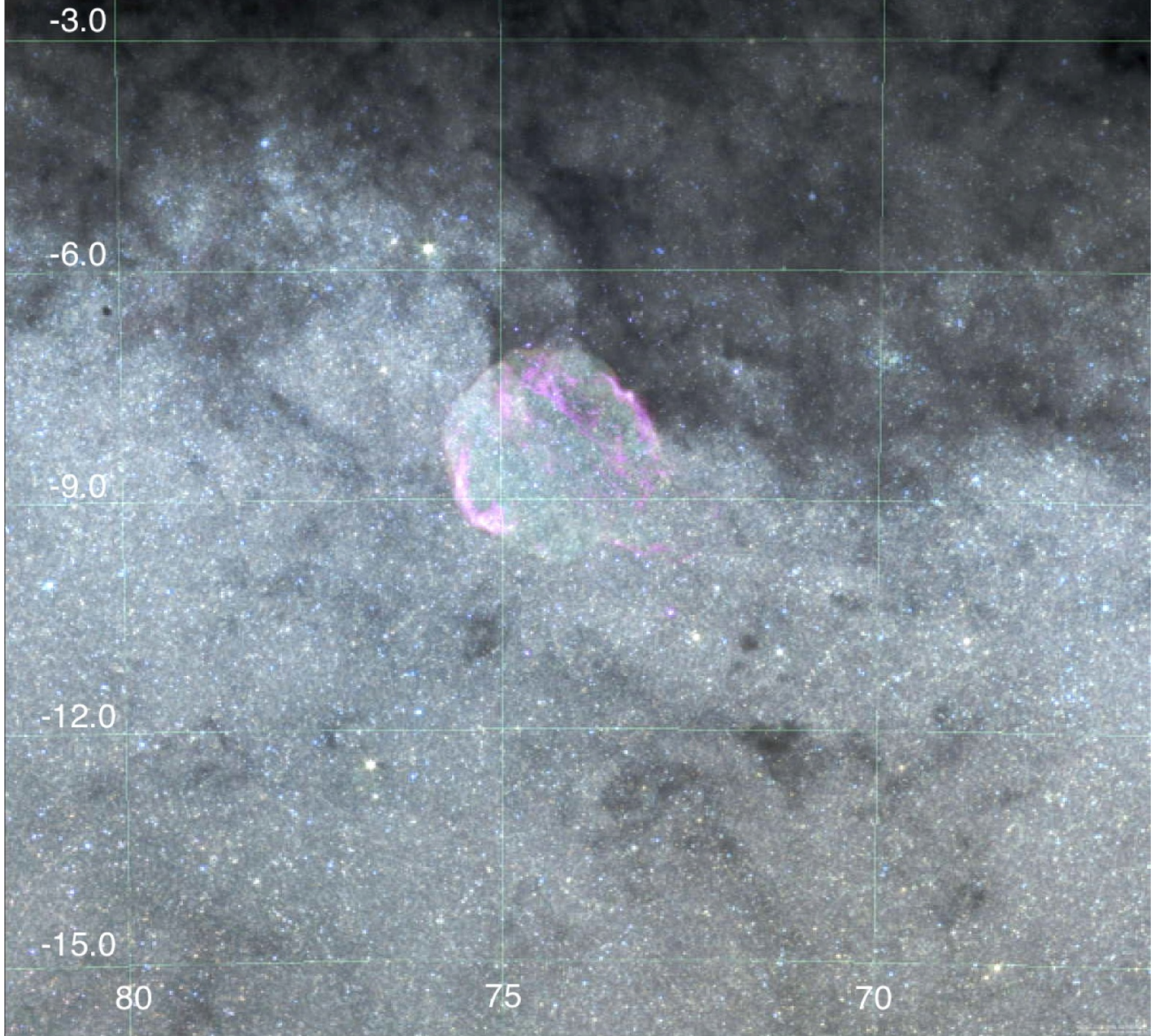


FIG. 6.— A wide-angle composite image made from optical Mellinger RGB images, Planck 857 GHz infrared data (gray), *GALEX* UV images (pink) and *ROSAT* X-ray images (white) of the Milky Way region around the Cygnus Loop. Galactic coordinates are shown. The remnant's brightest optical and X-ray emission features can be seen immediately adjacent to local dust clouds.

cloud in this region which was given a small outward velocity by the Cygnus Loop's progenitor star's ionizing radiation. A similar analysis was subsequently proposed for the remnant's southeastern limb (Leahy 2005). In both regions, interstellar clouds were proposed to be immediately adjacent to the remnant.

From a deep optical survey of the remnant's emission structure, Levenson et al. (1998) concluded the remnant's brightest optical emissions trace interactions of its blast wave with dense interstellar clumps. They found faint nonradiative, Balmer-dominated shock emission filaments forming a nearly circular and complete shell around the remnant's northern region with a radius of 1.9 degrees. They argued that the remnant's bright optical emission arising from radiative shocks are only seen where the blast wave encounters denser inhomogeneities in the local interstellar medium, and it is these interac-

tions which dominate the remnant's global appearance and evolution.

4.3.2. A Multi-wavelength Analysis

In order to investigate the interstellar environment around the Cygnus Loop, we constructed a series of multi-wavelength composite images of its neighboring regions using on-line data archives. These included Planck infrared images (Planck Collaboration et al. 2014), Wide-field Infrared Survey Explorer (*WISE*) data (Wright et al. 2010), *ROSAT* HRI and PSPC X-ray images, optical survey images including the Digital Sky Survey (DSS2) and the Mellinger survey (Mellinger 2009), and near UV image data from the Galaxy Evolution Explorer (*GALEX*) (Morrissey et al. 2007).

Figure 6 shows a roughly 12×15 degree wide composite image of the Milky Way around the Cygnus Loop covering Galactic coordinates $l = 66^\circ$ to 82° , $b = -2.8^\circ$

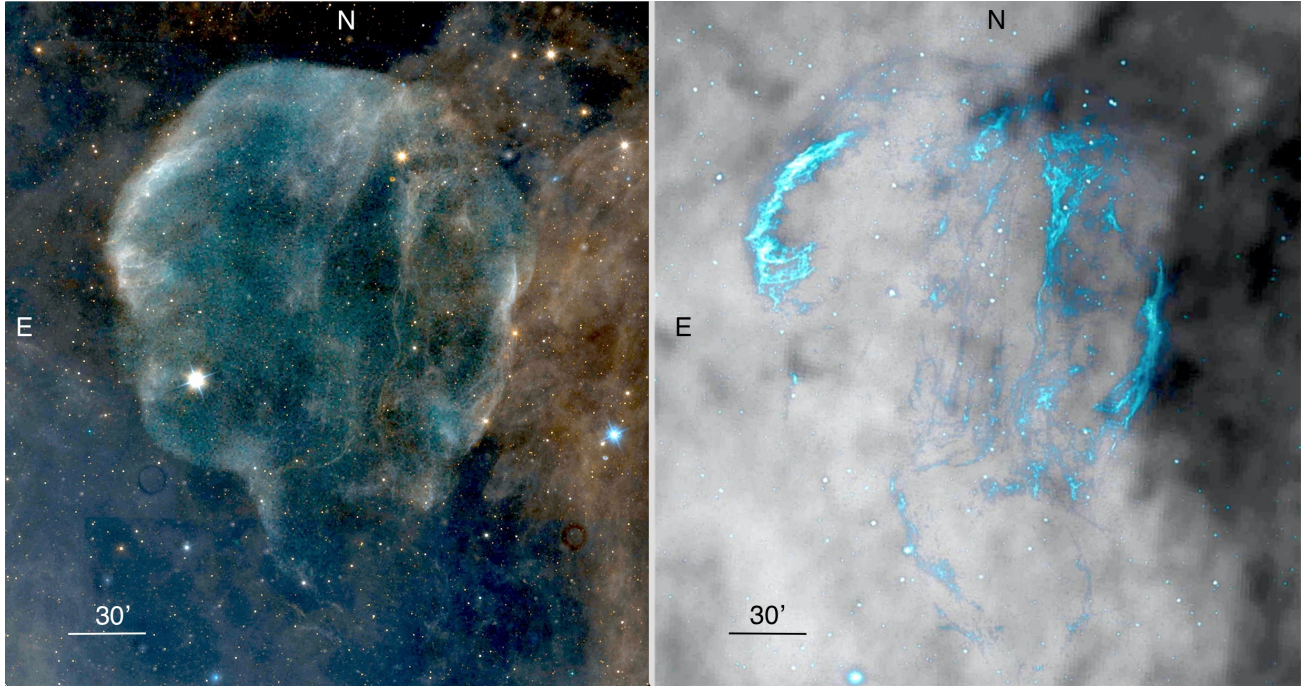


FIG. 7.— **Left Panel:** Composite positive image made from *ROSAT* X-ray (blue), *GALEX* UV (white), and *WISE* 12 & 22 μm infrared data (blue and red) highlighting the positional coincidence of the Cygnus Loop's X-ray and UV emissions with local dust clouds, and the remnant's expansion northward toward a region relatively clear of interstellar clouds. **Right Panel:** Composite image made from *Planck* 857 GHz (gray) data and *GALEX* UV data (positive blue) showing clouds all along the Cygnus Loop's eastern nebulae, plus a small cloud one degree south of NGC 6995 coincident with the remnant's small isolated southeastern emission knot.

to -15.5° , constructed from *Planck* 857 GHz, *ROSAT* PSPC, *GALEX* UV, and Mellinger images. This composite relates the projected locations of the remnant's X-ray and optical emissions with interstellar dust clouds.

The image shows that the remnant, located well off the Galactic plane between Galactic latitudes -6.9° to -9.8° , is situated in a broad channel largely empty of dust clouds, bounded on its western limb by a large, extended dust cloud stretching roughly from $l = 69^\circ$ to 75° . Eastern edges of this cloud coincide with the remnant's bright western and northwestern nebulosities, namely NGC 6960 and Pickering's Triangle. Smaller, less dense dust clouds near $l = 76^\circ, b = -9^\circ$ appear to coincide with the remnant's eastern X-ray and optical emissions, namely NGC 6992, NGC 6995, and IC 1340.

Additional composite images showing the interstellar medium around the Cygnus Loop using *WISE*, *GALEX*, *ROSAT*, and *Planck* data are shown in Figure 7, but now in an equatorial coordinate format. The left panel shows the remnant's *ROSAT* X-ray, *GALEX* UV and *WISE* infrared emissions in relation to projected locations of infrared emission from dust clouds. Especially notable is the presence of dust clouds along most of the remnant's western limb. The appearance of the remnant's emission relative to these clouds gives the impression that the remnant lies on the near side of these clouds. This is supported by the small extension or bulge of remnant's X-ray emitting shock front to the west of the northern tip of NGC 6960. We also note that the remnant's seemingly greater expansion to the north coincides with a region relatively free of significant interstellar clouds.

The other multi-wavelength composite shown in the right panel of Figure 7 reveals excellent correlation be-

tween the remnant's bright radiative UV and optical emission nebulae and projected locations of dust clouds. This includes dust clouds all along the remnant's bright eastern nebulosities, plus a small dust cloud coincident with the remnant's southeastern emission knot roughly one degree south of NGC 6995 that has been studied by Fesen et al. (1992), Graham et al. (1995), and Levenson & Graham (2001).

Although there is considerable evidence for direct cloud interaction along the Cygnus Loop's western limb (Levenson et al. 1996), there has not been previously published data pointing to specific dense clouds correlated with the remnant's other strong X-ray/UV/optical emission features such as Pickering's Triangle, NGC 6992 or NGC 6995. The locations of the dust clouds seen in Figures 6 and 7 greatly clarifies where and why the remnant looks the way it does across many wavelengths.

Using X-ray data and deep optical images covering the entire remnant, Levenson et al. (1998) attempted to construct a three-dimensional picture of the Cygnus Loop. They concluded that dense clouds and atomic gas together form the walls of a cavity in which the SN occurred. However, the composite images shown in Figures 6 and 7 make it clear that the “cavity” is simply a region relatively free of interstellar clouds.

We agree with Levenson et al.'s suggestion that a large cloud located along the rear of the remnant is responsible for its western limb emission since it is consistent with our distance estimate for the remnant centre vs. that of the B7 star. However, they claim that the cloud that is the cause for the bright northeastern emission is also on the far side, whereas we find evidence for the remnant's eastern emissions to be closer than emission along the

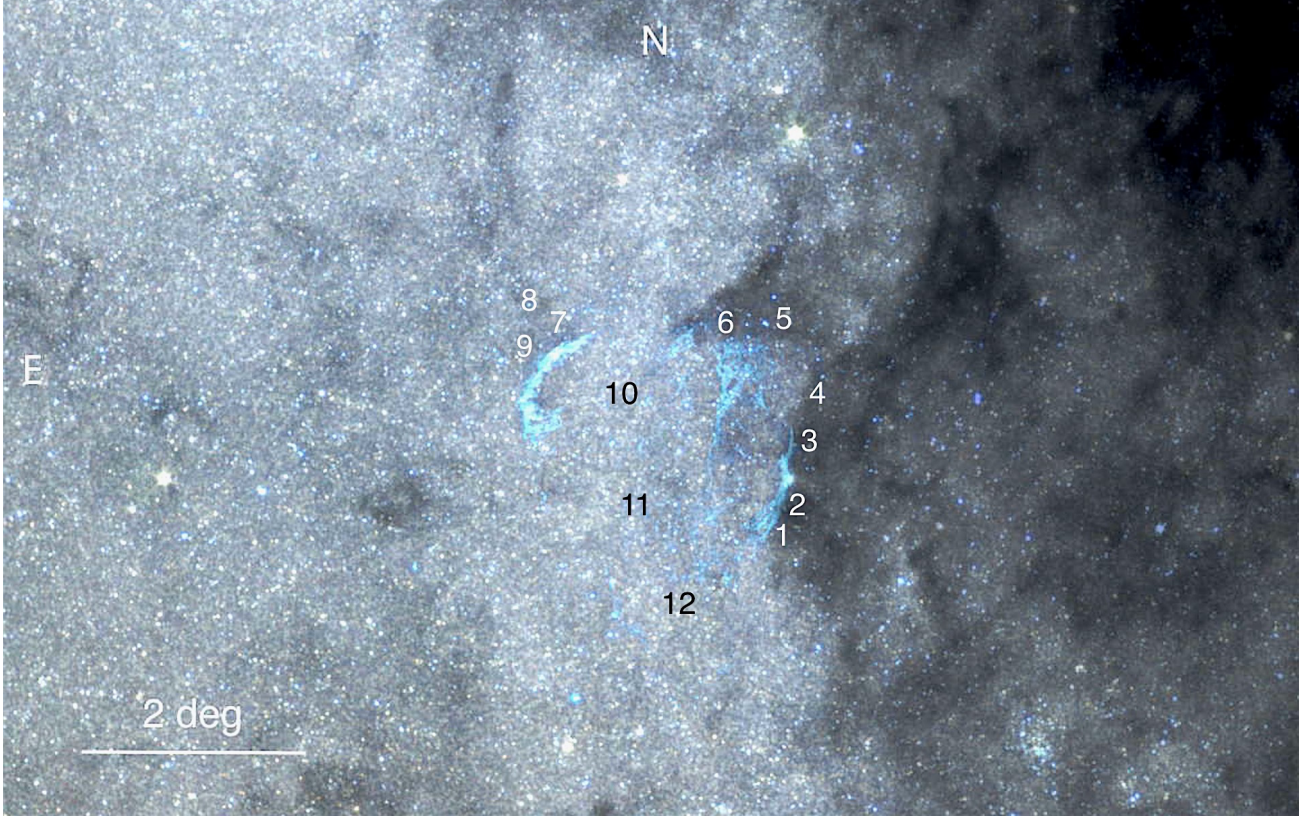


FIG. 8.— Composite image made from optical Mellinger RGB images (white), Planck infrared (gray) and GALEX UV (blue) data showing the presence of interstellar dust clouds projected along all of the remnant's bright optical and UV nebulosities. Marked are the 12 regions where reddening measurements were made using Pan-STARRS and 2MASS data on cumulative dust reddening with distance.

west and northwestern limbs.

One can test the idea that projected coincidences of these dust clouds do, in fact, signal interactions of the remnant's shock by using the new distance described above along with reddening versus distance estimates toward these clouds. Figure 8 shows 12 regions for which we obtained reddening values as a function of distance from the three-dimensional maps presented in Green et al. (2015) which utilized Pan-STARRS (Schlafly et al. 2014) and 2MASS (Skrutskie et al. 2006) photometry². Figure 8 also highlights again the projected locations of the Cygnus Loop's optical and UV bright nebulae relative to interstellar dust clouds and its position inside a broad N-S channel largely empty of interstellar clouds.

Measured $E(B - V)$ values for 450, 550, 650, 750, 850, and 950 pc for the 12 regions marked in Figure 8 are listed in Table 4. The sharp rise of extinction around 650 to 750 pc along the remnant's western limb (Regions 1-4) is presumably due to the molecular dust cloud the remnant is physically encountering. This rise is consistent with our derived 735 ± 25 pc distance. In like fashion, the reddening measurements to the northwestern clouds (Regions 5 & 6) and the fainter northeastern clouds (Regions 7-9) are also consistent with distances in excess of $\simeq 550$ pc. In contrast, the reddening measurements taken for projected regions toward the centre of remnant (Regions 10-12) show reddening values that only slowly increase with distance out to 950 pc.

It should be noted that these reddening measurements support the view that the B7 star lies inside the remnant as proposed by Fesen et al. (2018). Moreover, since reddening measurements for all 12 locations are found to be relatively low (< 0.13) out to 550 pc, distances to the Cygnus Loop of less than $\simeq 600$ pc are now firmly excluded. Finally, as mentioned above and discussed by Fesen et al. (2018), the presence of some of the remnant's shock filaments up to 30' farther to the west of NGC 6960 (see Fig. 4 in Fesen et al. 1992) suggests the remnant lies close to the near side of the western molecular cloud.

Interaction of the remnant's blast wave with local clouds along its eastern limb appears likely to have occurred relatively recently. Hester et al. (1986) used the presence of optical [O III] line emission behind a Balmer filament along the remnant's eastern limb to conclude that the remnant's shock hit a wall of denser gas a few hundred years ago. Shull & Hippelien (1991) cited X-ray emission just outside the remnant's eastern optical emission filaments to suggest that the cloud was encountered less than 1000 yr ago.

In summary, we find that the long suspected SN progenitor generated cavity walls appear, in fact, to be simply discrete interstellar clouds in the remnant's vicinity. Rather than invoking a low-density, progenitor wind-driven cavity, we find the remnant to be located in a broad region some eight degrees off the Galactic plane that is relatively free of interstellar clouds.

Specifically, we conclude that the remnant's gross morphology is due to the supernova's blast wave encounter-

² <http://argonaut.skymaps.info>

TABLE 4
REDDENING E(B-V) VALUES VS. DISTANCE FOR DUST CLOUDS AROUND THE CYGNUS LOOP

| Region | Number | RA | Dec | 450 pc | 550 pc | 650 pc | 750 pc | 850 pc | 950 pc |
|-------------------------|--------|------------|-----------|--------|--------|--------|--------|--------|--------|
| Western Molecular Cloud | 1 | 20:45:39.2 | +30:11:50 | 0.06 | 0.06 | 0.07 | 0.08 | 0.21 | 0.41 |
| | 2 | 20:45:22.5 | +30:31:45 | 0.03 | 0.04 | 0.08 | 0.32 | 0.42 | 0.42 |
| | 3 | 20:45:02.0 | +31:02:30 | 0.07 | 0.10 | 0.11 | 0.13 | 0.25 | 0.46 |
| | 4 | 20:44:39.3 | +31:28:15 | 0.05 | 0.05 | 0.10 | 0.34 | 0.43 | 0.45 |
| North West Clouds | 5 | 20:46:46.5 | +32:11:45 | 0.08 | 0.13 | 0.21 | 0.21 | 0.25 | 0.26 |
| | 6 | 20:48:24.1 | +32:09:15 | 0.04 | 0.11 | 0.19 | 0.25 | 0.29 | 0.30 |
| North East Clouds | 7 | 20:55:51.0 | +32:00:00 | 0.06 | 0.08 | 0.09 | 0.11 | 0.13 | 0.14 |
| | 8 | 20:57:18.0 | +32:13:30 | 0.09 | 0.10 | 0.12 | 0.14 | 0.16 | 0.17 |
| | 9 | 20:57:24.0 | +31:56:30 | 0.05 | 0.07 | 0.08 | 0.10 | 0.12 | 0.15 |
| Central Regions | 10 | 20:53:10.0 | +31:25:00 | 0.05 | 0.06 | 0.07 | 0.08 | 0.08 | 0.09 |
| | 11 | 20:53:44.0 | +30:22:00 | 0.04 | 0.05 | 0.05 | 0.06 | 0.06 | 0.07 |
| | 12 | 20:50:59.0 | +29:25:00 | 0.06 | 0.06 | 0.06 | 0.07 | 0.07 | 0.07 |

ing a large molecular cloud off to its west giving rise to NGC 6960, smaller discrete clouds off to the east and northeast resulting in NGC 6992, NGC 6995, and IC 1340, and relatively dense clouds to the northwest resulting in Pickering's Triangle and neighboring nebulae. Although X-ray abundance data suggests the Cygnus Loop is the remnant of a high-mass progenitor star, there is no need to propose a wind-driven cavity to explain the remnant's low density interior but relatively dense emission limbs.

4.4. The Nature of the Remnant's Southern Blowout

Finally, we address the nature of the southern blowout region which marks a significant departure from the remnant's otherwise fairly spherical morphology (see Fig. 1). The blowout region's optical emission is better seen in Figure 9 which shows a mosaic of H α images taken with the 0.6 m Burrell Schmidt telescope at Kitt Peak as part of a survey of the remnant's optical structure (see Patnaude et al. 2002 for details). Although viewed most often as a breakout of the remnant's expansion into a lower density region to the south (Levenson et al. 1998; Aschenbach & Leahy 1999), or possibly the wake left behind the high-mass progenitor as it moved northward (Meyer et al. 2015), there have been recent suggestions that it constitutes a completely separate remnant.

Based on radio continuum and polarization mapping at 2695 MHz that showed a significantly larger percentage of polarization in the blowout region compared to the remnant's northern part, Uyaniker et al. (2002) argued that the blowout actually represented a separate SNR interacting with the Cygnus Loop. In support of this scenario, they cited the presence of a possible neutron star near the centre of the blowout (Miyata et al. 2001), and differences between the northern and southern parts of the Cygnus Loop in terms of optical and X-ray emissions. Although they noted difficulties explaining the lack of strong X-ray emission in the overlapping and presumed interacting region, they concluded that it was not just two SNRs seen in superposition, but actually in physical contact.

Follow-up radio polarization studies by Sun et al. (2006) and West et al. (2016) confirmed large differences in polarization characteristics between the northern and southern portions of the Cygnus Loop, supporting the notion of two separate remnants. However, an X-ray study by Uchida et al. (2009) found no evidence in X-rays

that the blowout region constitutes a separate remnant.

Likewise, there is no indication from optical images that the lower portion of the Cygnus Loop's emission is separate or distinct from the rest of the remnant (see Fig. 9). The remnant's southern filamentary features connect to filaments in the blowout region, with the Cygnus Loop's highly curved southeastern shock front showing an abrupt cutoff at the intersection with the blowout region.

Moreover, the blowout region has its longer N-S axis and its southernmost tip in rough alignment with the centre line of the Cygnus Loop's main shell. This orientation is especially clear in X-ray maps of the remnant (Levenson et al. 1997; Aschenbach & Leahy 1999) and is not unlike that expected for a blowout of the remnant's shock front encountering a lower density interstellar region.

Also as can be seen in Figure 9, there is a large secondary blowout off the western side of the main blowout. The location of this secondary blowout roughly coincides with a break in the southern extent of the western molecular cloud (see Fig. 7) suggesting the blowout is at the same distance as the Cygnus Loop.

Consequently, we find no morphological evidence to support a second SNR scenario. This conclusion is strengthened by the lack of X-ray emission at a presumed interface region where two separate SNRs would be interacting. Thus we conclude, as did Ku et al. (1984), that the southern blowout is simply the result of the remnant's shock encountering a low density region ($n_0 < 0.1 \text{ cm}^{-3}$) more than nine degrees off the Galactic plane relatively absent of interstellar clouds.

5. CONCLUSIONS

While the Cygnus Loop is among the best studied Galactic supernova remnants, its distance has long been uncertain. Here we present the first detections of high-velocity interstellar absorptions of Na I and Ca II seen in the spectra of stars with projected locations within the remnant's boundary. These detections, along with the recent discovery of a B7 star, BD+31 4224, lying either inside and/or interacting directly with the remnant's expanding blast wave along the Cygnus Loop's northwest limb (Fesen et al. 2018), are used to set the most robust distance estimate to the remnant. Our findings are summarized below.

1) Moderate-dispersion spectra of three stars with projected locations toward the remnant reveal the first de-

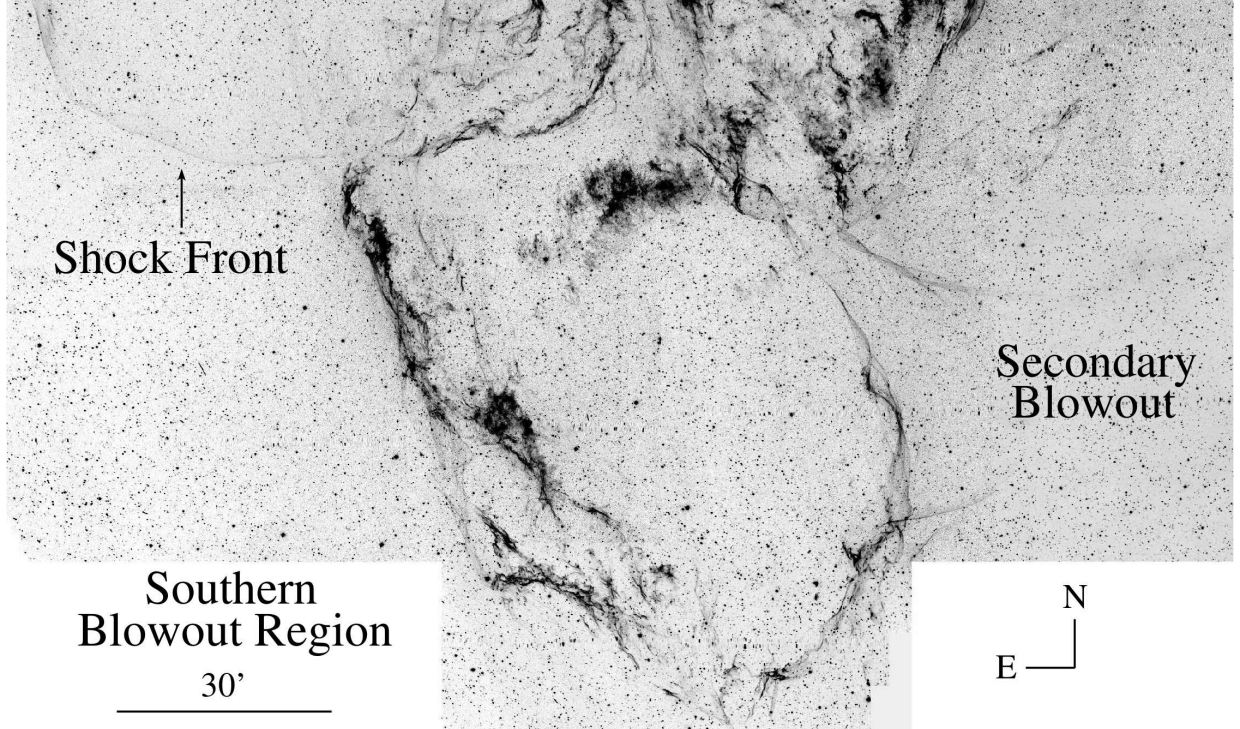


FIG. 9.— Deep H α image of the Cygnus Loop’s southern blowout region showing a secondary blowout structure off to the west.

tections of Na I 5890,5896 Å and Ca II 3934 Å absorption features associated with the remnant’s expanding shell. Measured LSR velocities range from -160 to $+240$ km s $^{-1}$.

2) We estimate the centre of the Cygnus Loop lies at a distance of 735 ± 25 pc based on the detection of high-velocity Na I absorptions in these three background stars, combined with the distance to the B7 star interacting with the remnant’s shock. We further find that the remnant is likely aspherical in shape, with its eastern limb nearer to us than its northwestern limb, with a diameter $\simeq 37$ pc.

3) Using our new estimated distance for the Cygnus Loop, we calculate several fundamental physical properties of the remnant which are in good agreement with inferred values reported from numerous previous studies (Table 3).

4) From inspection of multi-wavelength composite images, we find the Cygnus Loop’s morphology to be the result of its location far off the Galactic plane in a relatively low-density region in between local interstellar clouds. The interaction of the remnant’s blast wave with these clouds explains the locations of all its major optical and UV emission nebulae. Consequently, we propose that the Cygnus Loop is not a remnant inside a progenitor wind-driven, low-density cavity but rather lies in an extended, low-density region in between a dense molecular cloud to its west and northwest, with smaller clouds to its east and northeast.

5) These composite images along with deep H α images show no evidence supporting the notion that the Cygnus Loop’s southern blowout region is a separate SNR. Instead, the blowout is just what it appears to be: a blowout of the Cygnus Loop’s blast wave toward a low-density region largely absent of interstellar clouds.

Finally, we note the star, TYC 2688-2556-1, identified

by Boubert et al. (2017) as a possible runaway former companion of the Cygnus Loop’s progenitor at estimated distances around 430 pc (Gaia DR2) is unlikely if our estimate of $\simeq 735$ pc is correct. Likewise, the pulsar wind nebula candidate discovered by Katsuda et al. (2012) in the remnant’s southern blowout region, if physically related to the Cygnus Loop, would require a transverse velocity in excess of 1200 km s $^{-1}$, quite high but still lower than their estimate of 1850 km s $^{-1}$ assuming a distance of 540 pc and an age of 10,000 yr.

We thank the MDM Observatory staff for their assistance and rapid instrument re-configuration, and Ronald Downes and Debra Wallace for help in constructing an H α survey of the Cygnus Loop. This research was made possible in part by funds from NASA’s SpaceGrant, the Guarini School of Graduate and Advanced Studies at Dartmouth, and is part of RAF’s Archangel Research Program. We have made use of data from the European Space Agency (ESA) mission *Gaia* (<https://www.cosmos.esa.int/gaia>), processed by the *Gaia* Data Processing and Analysis Consortium (DPAC, <https://www.cosmos.esa.int/web/gaia/dpac/consortium>). Funding for the DPAC has been provided by national institutions, in particular the institutions participating in the *Gaia* Multilateral Agreement. This research has also made use of the SIMBAD database, operated at CDS, Strasbourg, France.

REFERENCES

Arendt, R. G., Dwarka, E., & Leisawitz, D. 1992, *ApJ*, 400, 562

Aschenbach, B., & Leahy, D. A. 1999, *A&A*, 341, 602

Ballet, J., Arnaud, M., & Rothenflug, R. 1984, *A&A*, 133, 357

Blair, W. P., Sankrit, R., & Raymond, J. C. 2005, *AJ*, 129, 2268

Blair, W. P., Sankrit, R., Torres, S. I., Chayer, P., & Danforth, C. W. 2009, *ApJ*, 692, 335

Bok, B. J., & Warwick, C. 1957, *AJ*, 62, 323

Boubert, D., Fraser, M., Evans, N. W., Green, D., & Izzard, R. G. 2017, *A&A*, 606, A14

Braun, R., & Strom, R. G. 1986, *A&A*, 164, 208

Chamberlain, J. W. 1953, *ApJ*, 117, 399

Charles, P. A., Kahn, S. M., & McKee, C. F. 1985, *ApJ*, 295, 456

Cox, D. P. 1972, *ApJ*, 178, 169

de Noyer, L. K. 1975, *ApJ*, 196, 479

Doroshenko, V. T. 1970, *Soviet Ast.*, 14, 237

Duncan, J. C. 1923, *ApJ*, 57, 137

Falle, S. A. E. G., & Garlick, A. R. 1982, *MNRAS*, 201, 635

Fang, J., Yu, H., & Zhang, L. 2017, *MNRAS*, 464, 940

Fesen, R. A., Kwitter, K. B., & Downes, R. A. 1992, *AJ*, 104, 719

Fesen, R. A., Neustadt, J. M. M., Black, C., & Milisavljevic, D., 2018, *MNRAS*, 475, 3996

Gaia Collaboration, Brown, A. G. A., Vallenari, A., et al. 2018, *arXiv:1804.09365*

Graham, J. R., Levenson, N. A., Hester, J. J., Raymond, J. C., & Petre, R. 1995, *ApJ*, 444, 787

Green, G. M., Schlafly, E. F., Finkbeiner, D. P., et al. 2015, *ApJ*, 810, 25

Hester, J. J., Danielson, G. E., & Raymond, J. C. 1986, *ApJ*, 303, L17

Hester, J. J., Raymond, J. C., & Blair, W. P. 1994, *ApJ*, 420, 721

Høg, E., Fabricius, C., Makarov, V. V., et al. 2000, *A&A*, 355, L27

Hubble, E. P. 1937, *Carnegie Institution of Washington Yearbook 1936-1937*, Report from the Mount Wilson Observatory by W.S. Adams & F.H. Sears, p189.

Katsuda, S., Tsunemi, H., Mori, K., et al. 2012, *ApJ*, 754, L7

Ku, W. H.-M., Kahn, S. M., Pisarski, R., & Long, K. S. 1984, *ApJ*, 278, 615

Leahy, D. A. 2003, *ApJ*, 586, 224

Leahy, D. A. 2005, *AJ*, 130, 165

Levenson, N. A., Graham, J. R., Hester, J. J., & Petre, R. 1996, *ApJ*, 468, 323

Levenson, N. A., Graham, J. R., Aschenbach, B., et al. 1997, *ApJ*, 484, 304

Levenson, N. A., Graham, J. R., Keller, L. D., & Richter, M. J. 1998, *ApJS*, 118, 541

Levenson, N. A., & Graham, J. R. 2001, *ApJ*, 559, 948

Long, K. S., Blair, W. P., Vancura, O., et al. 1992, *ApJ*, 400, 214

McCrory, R., & Snow, T. P., Jr. 1979, *ARA&A*, 17, 213

McEntaffer, R. L., & Brantseg, T. 2011, *ApJ*, 730, 99

McKee, C. F., & Cowie, L. L. 1975, *ApJ*, 195, 715

Medina, A. A., Raymond, J. C., Edgar, R. J., et al. 2014, *ApJ*, 791, 30

Mellinger, A. 2009, *PASP*, 121, 1180

Meyer, D. M.-A., Langer, N., Mackey, J., Velázquez, P. F., & Gusdorf, A. 2015, *MNRAS*, 450, 3080

Minkowski, R. 1958, *Reviews of Modern Physics*, 30, 1048

Miyata, E., & Tsunemi, H. 1999, *ApJ*, 525, 305

Miyata, E., Ohta, K., Torii, K., et al. 2001, *ApJ*, 550, 1023

Morrissey, P., Conrow, T., Barlow, T. A., et al. 2007, *ApJS*, 173, 682

Oort, J. H. 1946, *MNRAS*, 106, 159

Patnaude, D. J., Fesen, R. A., Raymond, J. C., et al. 2002, *AJ*, 124, 2118

Planck Collaboration, Abergel, A., Ade, P. A. R., et al. 2014, *A&A*, 571, A11

Rappaport, S., Doxsey, R., Solinger, A., & Borken, R. 1974, *ApJ*, 194, 329

Raymond, J. C., Edgar, R. J., Ghavamian, P., & Blair, W. P. 2015, *ApJ*, 805, 152

Raymond, J. C., Hester, J. J., Cox, D., et al. 1988, *ApJ*, 324, 869

Raymond, J. C., Ghavamian, P., Sankrit, R., Blair, W. P., & Curiel, S. 2003, *ApJ*, 584, 770

Ross, F. E. 1931, *ApJ*, 74, 85

Routly, P. M., & Spitzer, L., Jr. 1952, *ApJ*, 115, 227

Salvesen, G., Raymond, J. C., & Edgar, R. J. 2009, *ApJ*, 702, 327

Schlafly, E. F., Green, G., Finkbeiner, D. P., et al. 2014, *ApJ*, 789, 15

Scoville, N. Z., Irvine, W. M., Wannier, P. G., & Predmore, C. R. 1977, *ApJ*, 216, 320

Shull, P., Jr., & Hippelein, H. 1991, *ApJ*, 383, 714

Skrutskie, M. F., Cutri, R. M., Stiening, R., et al. 2006, *AJ*, 131, 1163

Sun, X. H., Reich, W., Han, J. L., Reich, P., & Wielebinski, R. 2006, *A&A*, 447, 937

Tucker, W. H. 1971, *Science*, 172, 372

Vallerga, J. V., Vedder, P. W., Craig, N., & Welsh, B. Y. 1993, *ApJ*, 411, 729

van Dokkum, P. G. 2001, *PASP*, 113, 142

Uchida, H., Tsunemi, H., Katsuda, S., et al. 2009, *PASJ*, 61, 503

Uyaniker, B., Reich, W., Yar, A., Kothes, R., & Fürst, E. 2002, *A&A*, 389, L61

Welsh, B. Y., Sallmen, S., Sfeir, D., & Lallement, R. 2002, *A&A*, 391, 705

Wenger, M., Ochsenbein, F., Egret, D., et al. 2000, *A&AS*, 143, 9

West, J., Safi-Harb, S., Reichardt, I., et al. 2016, *Supernova Remnants: An Odyssey in Space after Stellar Death*, 35

Wolf, M. 1923, *Astronomische Nachrichten*, 219, 109

Wright, E. L., Eisenhardt, P. R. M., Mainzer, A. K., et al. 2010, *AJ*, 140, 1868

Zacharias, N., Urban, S. E., Zacharias, M. I., et al. 2004, *AJ*, 127, 3043